RSC Advances

ROYAL SOCIETY OF CHEMISTRY

www.rsc.org/advances

RSC Advances

RSCPublishing

ARTICLE

Inhibiting the interaction between FeO and Al_2O_3 during chemical looping production of hydrogen

.Cite this: DOI: 10.1039/x0xx00000x

Wen Liu,*[a] Mohammad Ismail,[a] Matthew T. Dunstan,[b] Wenting Hu,[c] Zili Zhang,[d] Paul S. Fennell,[d] Stuart A. Scott[a] and J. S. Dennis[c],

Received 00th January 2012,
Accepted 00th January 2012

DOI: 10.1039/x0xx00000x

www.rsc.org/

Hydrogen of high purity can be produced by chemical looping using iron oxide as an oxygen carrier and making use of the reaction between steam and either iron or FeO. However, this process is viable only if the iron oxide can be cycled between the fully-oxidised and fully-reduced state many times. This can be achieved if the iron oxide is supported on refractory oxides such as alumina. Unfortunately, the interaction between alumina and oxides of iron to form $FeAl_2O_4$ hinders the kinetics of the reactions essential to the production of hydrogen, *viz*. the reduction of Fe(II) to metallic iron by a mixture of CO and CO_2 prior to the oxidation by steam. Here, oxygen carriers containing Fe_2O_3 and Al_2O_3 were doped with Na_2O and, or, MgO, in order to inhibit the formation of $FeAl_2O_4$ by forming $NaAlO_2$ or $MgAl_2O_4$, respectively. The performance of the modified oxygen carriers for producing hydrogen, *i.e*. cyclic transitions between Fe_2O_3 (or Fe_3O_4) and metallic Fe at 1123 K were investigated. It was found that the interaction between FeO and Al_2O_3 was successfully mitigated in oxygen carrier containing Mg, with an Al : Mg ratio of 2, resulting in consistently stable and high capacity for producing hydrogen by chemical looping, whether or not the material was oxidised fully in air on each cycle. However, the oxygen carrier without Mg only remained active when a step to oxidise the sample in air was included in each cycle. Otherwise it progressively deactivated with cycling, showing substantial interaction between Al_2O_3 and oxides of Fe.

1. Introduction

Hydrogen is a potential fuel for a low-carbon economy, provided it can be manufactured with minimal release of CO_2 to the atmosphere. Generally, to generate hydrogen, carbonaceous fuels need to be consumed, usually *via* large-scale, energy-intensive processes such as steam-methane reforming. Where the hydrogen is to be used in polymeric-electrolyte-membrane fuel cells; an additional process is required to purify the hydrogen to avoid poisoning of the Pt electrodes by the low concentrations of CO which contaminate the product of steam-methane reforming.[1] However, CO may be less of a problem in other types of fuel cells, *e.g*. solid-oxide fuel cells or solid molten carbonate fuel cells.[1] An alternative process, capable of producing pure hydrogen directly from carbonaceous fuels, at small to medium scales with simultaneous capture of CO_2, is chemical looping hydrogen production.[2]

Chemical looping techniques rely on the ability of transition metal oxides to transport oxygen from an oxidising environment to a reducing environment. When CO is used as a reductant and the oxygen in air is used as an oxidant, the reactions can be generalised:

CO reduction: $MeO_{x(s)} + yCO_{(g)} \rightarrow MeO_{x-y(s)} + yCO_{2(g)}$ (1)

Air oxidation: $MeO_{x-y\ (s)} + O_{2(g)} \rightarrow MeO_{x(s)}$ (2)

where MeO_x and MeO_{x-y} represent the oxidised and reduced forms of the transition metal oxide, referred to here, together with any supporting matrix, as the oxygen carrier. In this example, oxygen is transported from air by MeO_x to combust CO in a nitrogen-free environment, resulting in a stream of pure CO_2, which is suitable for carbon storage. Here, the additional cost associated with the separation of CO_2 from N_2 for carbon capture in conventional coal-fired power plants is avoided. In a variant of the above, if iron oxide is used as an oxygen carrier, hydrogen can be produced during the oxidation stage of the steam-iron process:

$3/4Fe_{(s)} + H_2O_{(g)} \rightleftharpoons 1/4Fe_3O_{4(s)} + H_{2(g)}$,

$\Delta H^o_{1123\ K} = -26.3$ kJ/mol (3)

originally patented by Messerschmitt[3]. Reed and Berg[4] proposed a system to produce pure hydrogen continuously using the steam-iron process, by circulating iron oxides between three interconnected fluidised bed reactors. In their process, the iron oxide oxygen carrier was subjected to repeated redox reactions, *i.e.* chemical looping. When synthesis gas, *e.g*. a mixture of CO and H_2 is used as a fuel, the reactions in the three-reactor system would be:

$3Fe_2O_{3(s)} + H_{2(g)} \rightleftharpoons 2Fe_3O_{4(g)} + H_2O_{(g)}$

$\Delta H^o_{1123\ K} = -5.9$ kJ/mol (4)

$1.202Fe_3O_{4(s)} + H_{2(g)} \rightleftharpoons 3.807Fe_{0.947}O_{(s)} + H_2O_{(g)}$

$\Delta H^o_{1123\ K} = +56.6$ kJ/mol (5)

$Fe_{0.947}O_{(s)} + H_{2(g)} \rightleftharpoons 0.947\ Fe_{(s)} + H_2O_{(g)}$

$\Delta H^o_{1123\ K} = -16.9$ kJ/mol (6)

$3Fe_2O_{3(s)} + CO_{(g)} \rightleftharpoons 2Fe_3O_{4(s)} + CO_{2(g)}$

$\Delta H^o_{1123\ K} = -40.8$ kJ/mol (7)

$1.202Fe_3O_{4(s)} + CO_{(g)} \rightleftharpoons 3.807Fe_{0.947}O_{(s)} + CO_{2(g)}$

$\Delta H^o_{1123\ K} = +34.9$ kJ/mol (8)

$Fe_{0.947}O_{(s)} + CO_{(g)} \rightleftharpoons 0.947\ Fe_{(s)} + CO_{2(g)}$

$\Delta H^o_{1123\ K} = -16.6$ kJ/mol (9)

$2Fe_3O_{4(s)} + 1/2O_{2(g)} \rightleftharpoons 3Fe_2O_{3(s)}$

$\Delta H^o_{1123\ K} = -237.2$ kJ/mol (10)

In the first reactor, *viz.* the fuel reactor, reactions (4) − (9) would be conducted, where haematite (Fe_2O_3) is reduced by CO and H_2 sequentially to magnetite (Fe_3O_4), wüstite ($Fe_{0.947}O$) and iron (Fe). Both wüstite and iron can be then oxidised by steam in the second reactor, *viz*. the steam reactor, according to the reverse of reactions (3) and (5). The solid product, magnetite, is further oxidised to haematite according to the exothermic reaction (10), in the third reactor, *viz*. the air reactor, which provides heat to the system. Overall, the chemical energy of the synthesis gas is used to produce hydrogen by splitting water *via* chemical looping of the iron oxide. Of course, the hydrogen used during the reduction is mixed with CO, whereas the hydrogen produced in this manner is effectively free from carbonaceous contamination, and has high purity.[2]

One of the major challenges in the production of hydrogen by chemical looping is the development of a stable oxygen carrier capable of being reduced and oxidised over many cycles without deactivation. When almost pure iron oxide (99 wt% haematite) is used as an oxygen carrier, the reduction of Fe_3O_4 to Fe in each cycle led to rapid deactivation within the first few cycles.[2] However, by limiting the extent of reduction to wüstite (FeO) in every cycle, a stable hydrogen yield could be obtained over more than 10 redox cycles.[2] Nevertheless, the transition between Fe and Fe_3O_4 produces about four times as much hydrogen as the transition between wüstite (FeO) and magnetite (Fe_3O_4), for a given mass of iron, so that reduction to iron is desirable to maximise yield. Further studies have shown that supporting the iron oxide on Al_2O_3 could stabilise the performance of iron-based oxygen carriers.[5–7] However, it was also found that hercynite, $FeAl_2O_4$, was inevitably formed in the presence of Al_2O_3 and this slowed down the rate of reduction of the supported iron oxide when the latter was reduced beyond Fe_3O_4.[8] Here, $FeAl_2O_4$ belongs to the spinel group of crystalline phases with a general formula of AB_2O_4, where the A-sites are typically occupied by divalent cations and B-sites by trivalent cations. On the other hand, it was hypothesised by Kidambi *et al*.,[7] that the formation and destruction of solid phases on each redox cycle might be important in maintaining the activity of the oxygen carrier. However, Liu *et al*.[9] have demonstrated the stabilising effect of a ZrO_2 support on the performance of iron oxide oxygen carriers for chemical looping hydrogen production. The support in this system is chemically stable, and no phases involving iron oxide are formed. Therefore, albeit desirable, it is not strictly necessary for there to be changes of phase to promote a carrier's stability over many cycles. Nevertheless, one drawback of using ZrO_2 as a support material for chemical looping is its high cost relative to common refractory materials, *e.g.* Al_2O_3.

To avoid the formation of $FeAl_2O_4$, several researchers have proposed using $MgAl_2O_4$ as a replacement for Al_2O_3 as a support material on the basis that it prevents spinel formation with the transition metal oxides for chemical looping combustion operations.[10–12] It was found that the use of $MgAl_2O_4$ (melting point = 2135ºC) as a support material gave both excellent mechanical strength and thermal resistance, whilst the reactivity of the active metal oxides for chemical looping combustion was preserved.[10–12] Interestingly, when CuO is used as a chemical looping agent, researchers have reported that the formation of the spinel phase $CuAl_2O_4$ is inhibited in the presence of trace amounts of alkali metals (*e.g.* Na and K).[13–15] The source of these alkali metal "contaminants" is most likely to be the Na- and K-dawsonites, *viz*. $NaAlCO_3(OH)_2$ and $KAlCO_3(OH)_2$, respectively, during the preparation of the oxygen carriers by co-precipitation.

The aim of the present study is to investigate the potential to use oxygen carriers containing a mixture of Fe_2O_3, Al_2O_3, Na_2O and, or, MgO for producing hydrogen by chemical looping, because the use of Na_2O and MgO could potentially inhibit the formation of $FeAl_2O_4$ by forming $NaAlO_2$ and $MgAl_2O_4$ with Al_2O_3 instead. Two oxygen carriers were synthesised: one containing oxides of Fe, Al and Na and another containing oxides of Fe, Mg, Al and Na. Both oxygen carriers were investigated under conditions which simulate the production of hydrogen by chemical looping. The formation and interaction of different phases of mixed oxides during repeated redox cycling were studied using *ex-situ* characterisation techniques.

2. Experimental

2.1. Preparation of oxygen carriers

The oxygen carriers containing (a) oxides of Fe, Al and Na, and (b) oxides of Fe, Mg, Al and Na are hereinafter referred to, respectively, as NAFO and NMAFO. Both oxygen carriers were synthesised using the method of co-precipitation with a slowly decreasing pH. In both cases, the precipitant used was an aqueous solution containing NaOH (≥ 98 wt%, Fisher Scientific) and Na_2CO_3 (≥ 99.5 wt%, Fisher Scientific) mixed at a molar ratio of 1:1 to give a total concentration of $[Na^+] \sim 4$ M. The precursors were aqueous solutions containing nitrates of Mg^{2+}, Al^{3+} and Fe^{3+}, *viz*. $Mg(NO_3)_2{\cdot}9H_2O$ (BioXtra, ≥98 wt%, Sigma-Aldrich), $Al(NO_3)_3{\cdot}9H_2O$ (ACS reagent, ≥98 wt%, Sigma-Aldrich) and $Fe(NO_3)_3{\cdot}9H_2O$ (ACS reagent, ≥98 wt%, Sigma-Aldrich), with a total cationic concentration of 2 M. The ratios of $[Mg^{2+}]$: $[Al^{3+}]$: $[Fe^{3+}]$ in the precursors for NAFO and NMAFO were 0: 1: 1.49 and 1: 2: 2.16, respectively. These ratios correspond to mass fractions of

Fe_2O_3 of 71.4% and 54.9%, respectively, in NAFO and NMAFO, if neither oxygen carriers contained Na^+ or any other metal elements. The ratio of $[Mg^{2+}]$: $[Al^{3+}]$ of 1: 2 for NMAFO corresponds to the stoichiometric formation of $MgAl_2O_4$, ignoring Fe. The total number of moles of NaOH and Na_2CO_3 in the alkali solution (the precipitant) was 3 times the total number of moles of metal ions (Mg^{2+}, Al^{3+} and Fe^{3+}) in the nitrate solution (the precursor).

The precipitation was undertaken isothermally at 373 K, at atmospheric pressure. During precipitation, the precursor was added at a constant rate of *ca*. 1 drop per second to a 1 L flask containing the alkali solution, which was stirred constantly at 600 rpm. The temperature of the solution in the flask was held constant at 100°C, below the point at which the slurry boiled. Loss of water by evaporation was prevented by condensing and refluxing all the vapour at the outlet of the flask. After the addition of the last drop of nitrate solution, the precipitate was kept stirred at 373 K for an additional 24 h. The final pH of the resulting slurry was found to be 10.0 ± 0.2. Then, the slurry was washed repeatedly with de-ionised water (with an ionic conductivity of ~20 μS cm^{-1}) until the ionic conductivity of the wash water fell below 120 μS cm^{-1}. Approximately 120 L of de-ionised water was used, over 4 exchanges, to wash each batch of precipitate which yielded 20 g of calcined oxygen carrier. The washed precipitates were filtered, dried at 353 K in air for 24 h, and fired at 1223 K for 3 h. The resulting cake of oxygen carrier was crushed and sieved to a size fraction of 300 – 425 μm for experiments in a packed bed reactor.

2.2. Characterisation of the solids

To characterise the crystalline phases in the solid samples, X-ray powder diffraction (XRD) were performed on a Panalytical X'Pert Pro diffractometer using Cu Kα radiation (wavelength = 1.5418 Å), operated at 40 kV and 40 mA. The angle of reflection, 2θ, was varied between 5 and 60º, at a rate of 0.0167° per step where each step takes 16.5 s. The diffraction patterns were collected at ambient temperature and atmosphere. The collected diffractograms were preliminarily inspected with the aid of reference patterns found in the Inorganic Crystal Structure Database (ICSD). Rietveld refinements were further performed on the collected diffractograms using GSAS with the graphical interface EXPGUI.[16,17] To investigate the elemental composition of the oxygen carriers, loose powders of the oxygen carriers were analysed by an S4 Explorer X-ray fluorescence spectrometer (XRF) system (Bruker AXS GmbH). The surface morphologies of the solid samples were inspected by a scanning electron microscope (NOVA NANOSEM, FEI), with a secondary electron detector, an accelerating voltage of 5 kV and probe current of 2 nA under high-vacuum (6×10^{-5} mbar). The samples were sputter-coated with Pt prior to examination by SEM. Energy-dispersive X-ray spectroscopy (EDS) analyses were performed on selected spots on the surface of the solid samples within the same SEM, using an accelerating voltage of 15 kV. The elemental composition at these spots was quantified using the collected EDS spectra and existing calibrations.

The oxygen content available for reduction and oxidation in the oxygen carriers was quantified by reducing the samples isothermally in a thermogravimetric analyser (TGA/DSC1, Mettler Toledo). In a typical TGA experiment, *ca*. 20 mg of fully oxidised sample was placed in a 70 μL alumina crucible, and heated to 1223 K at a rate of 20 K min^{-1} under a flow of N_2 (BOC Ltd.) of 50 mL min^{-1} (measured at 295 K, 1 atm). After degassing for one hour at 1123 K, an additional flow of 50 mL min^{-1} (measured at 295 K, 1 atm) of 5 vol.% H_2 in N_2 (Spectrashield, BOC Ltd.) was introduced to the reaction chamber for 10 h before cooling down in N_2 at a rate of −20 K min^{-1}. The change in mass of the samples was recorded and the mass fraction of Fe_2O_3 in the fully oxidised sample was calculated, as shown later in section 5.1.

To investigate the performance of the oxygen carriers, the samples were cycled under conditions suitable for producing hydrogen by chemical looping in a vertical packed bed. The wall of the tubular reactor (nominal *I.D.* = 9 mm) was made of recrystallised Al_2O_3 (>99 wt% purity, Multi-Lab Ltd.). The results of an earlier study by Liu *et al*.[9] confirm that the wall of the tube does not react with Fe-based oxygen carriers under chemical looping conditions, and can be therefore considered as inert. The packing arrangement, from top to bottom, consisted of the following layers of materials: (i) 10.0 g α-Al_2O_3 (1400 – 1700 μm), (ii) approximately 0.3 g of oxygen carrier particles (300 – 425 μm), (iii) 2.0 g of α-Al_2O_3 (300 – 425 μm), (iv) 2.0 g of α-Al_2O_3 (1400 – 1700 μm), and (v) a ceramic distributor plate. The distributor, consisting of three holes of diameter 1.5 mm each in triangular array, was cast using an Al_2O_3-based cement (AL/CS – chemical setting adhesive cement, Multi-lab Ltd.) inside the tube. Both ends of the alumina tube were fitted with brass fittings with Viton rubber O-rings acting as seals. The control and gas sampling system for the packed bed has been described elsewhere by Liu *et al*.[9].

During the cycling experiments in the packed bed, the temperature of the active bed was maintained at 1123 K. In each cycle, the gas supplied to the bed consisted successively of: (i) 5 min of reduction by 9.5 vol% CO in N_2 (BOC Ltd.), (ii) 2 min of N_2 purge (Air Liquide UK), (iii) 3 min of oxidation by 12 vol% CO_2 (Air Liquide UK) in N_2 and (iv) 1 min of N_2 purge and (v) 2 min of oxidation by air. Switching between the feed-gases was achieved using solenoid valves. In an additional set of experiments, the freshly-prepared oxygen carriers were cycled without step (v), in order to examine the presence of interaction between Al_2O_3 and oxides of Fe. Should there be interaction between Al_2O_3 and oxides of Fe, the absence of step (v) would result in a decay in reactivity and consequently deterioration in the conversion of solid over cycles, as shown by Kidambi *et al*.[7]. It should be noted that CO_2 was used in step (iii) to simulate the oxidation of reduced iron oxide by steam to produce hydrogen, because the equilibrium values of p_{CO_2}/p_{CO} and p_{H_2O}/p_{H_2} for the oxidation of Fe to wüstite and wüstite to Fe_3O_4 are similar at 1123 K,

where p_i stands for partial pressure of species *i*. The validity of using CO_2 to stimulate steam oxidation for chemical looping hydrogen cycles has also been experimentally confirmed by Liu *et al.*[9]. The flowrates of gases at the inlet were controlled and monitored using rotameters or mass flow sensors (Honeywell AWM5103VN). In all stages, the nominal gas flowrates were 1.5 L min^{-1} (measured at 295 K, 1 atm). For each sample, the oxygen carrier was cycled 20 times, with or without air-oxidation, *viz*. step (v). The effluent gas from the reactor was analysed by a non-dispersive infrared analyser (NDIR, Uras26, EL3020, ABB), which detects the mole fractions of CO and CO_2 in the range of 0 – 10 vol% and 0 – 12 vol%, respectively.

3. Results

3.1. Characterisation of the uncalcined precipitate

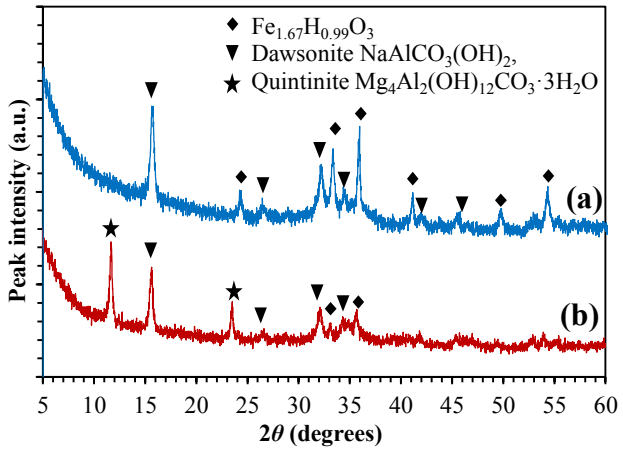

4.

5. Fig. 1 X-ray diffraction patterns of the precipitates during the preparation of (a) NAFO and (b) NMAFO, before thermal treatment. All diffraction peaks between 5° and 60° are identified and marked with the corresponding crystalline phases.

X-ray diffraction patterns of the precipitates were collected to investigate the crystalline phases formed during co-precipitation but before calcining at 1223 K; they are shown in Fig. 1. In Fig. 1a, it can be seen that the dried precipitate consisted of a mixture of $NaAlCO_3(OH)_2$ (dawsonite) and $Fe_{1.67}H_{0.99}O_3$, a dehydrated form of $Fe(OH)_3$. In Fig. 1b, the peaks at 11.7° and 23.5° are characteristic of the (0 0 2) and (0 0 4) planes, respectively, of $Mg_4Al_2(OH)_{12}CO_3{\cdot}3H_2O$ (quintinite). The fact that the position of the peaks of the quintinite phase matches closely a reference pattern of pure quintinite ($Mg_4Al_2(OH)_{12}CO_3{\cdot}3H_2O$, ICSD-182293) suggests that the trivalent sites in the quintinite phase contain little or no Fe^{3+}, *i.e.*, almost all Fe^{3+} precipitated in the form of $Fe(OH)_3$. Peaks of dawsonite are also seen in Fig. 1b, together with weak peaks of $Fe_{1.67}H_{0.99}O_3$. If there are no amorphous phases present, the precipitates of (a) NAFO and (b) NMAFO, should contain mixtures of (a) dawsonite and $Fe(OH)_3$ and (b) quintinite, dawsonite and $Fe(OH)_3$, respectively. In particular, for NAFO, the composition detected by XRD is also in agreement with the results of XRF shown in Table 1 below. Overall, all peaks in Fig. 1 can be indexed by $Fe_{1.67}H_{0.99}O_3$, dawsonite and quintinite.

The precipitates of both samples were also examined by SEM, and the images are shown in Fig. 2. Both images in Fig. 2 show large rod-shaped crystallites, which are characteristic of the dawsonite ($NaAlCO_3(OH)_2$) phase.[18] In Fig. 2(a), it can be seen that the precipitate also contains spherical agglomerates. Assuming no amorphous phase is present, these spherical agglomerates should be the dehydrated precipitate of $Fe(OH)_3$. Fig. 2(b) shows that the precipitates for NMAFO consist of a mixture of rod-shaped crystals and some small grains. Based on the results of XRD, the latter may be assigned to a mixture of quintinite and $Fe(OH)_3$.

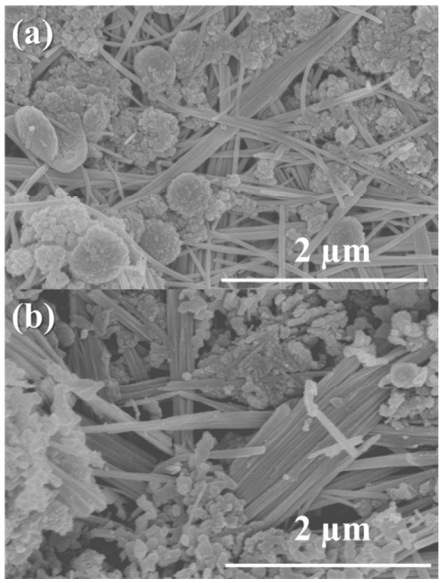

Fig. 2 Scanning electron micrographs of the precipitates during the preparation of (a) NAFO and (b) NMAFO.

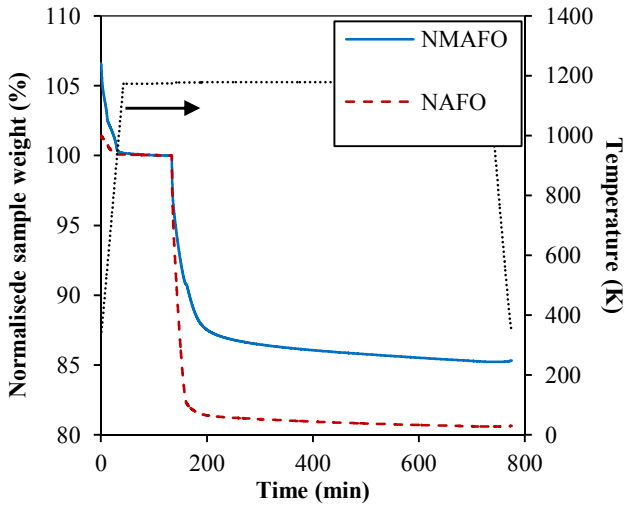

Fig. 3 Normalised sample mass versus time during the isothermal reduction of the freshly-prepared oxygen carriers at 950°C by H_2 in N_2.

5.1. Characterisation of the calcined precipitate

The mass fraction of the active iron oxide in the calcined precipitates, *i.e.* the freshly-prepared oxygen carriers, was determined by isothermal reduction of the calcined samples in a diluted stream of H_2 in N_2 at 1223 K in the TGA. The change in mass of the samples during reduction was rendered dimensionless:

$$\hat{m}_{red}(t) = m(t)/m(0), \quad (11)$$

where $m(0)$ is the mass of the sample just before reduction by H_2, at $t \sim 133$ min, when there was no further weight loss by dehydration and degassing of the solid sample. The resulting profiles of $\hat{m}_{red}(t)$ are shown in Fig. 3. Assuming complete reduction of the samples at the end of the experiment, $x_{Fe_2O_3}$, the mass fraction of Fe_2O_3 in the calcined oxygen carrier, was estimated using:

$$x_{Fe_2O_3} = [1 - \hat{m}_{red}(\infty)]/0.301, \quad (12)$$

where $\hat{m}_{red}(\infty)$ equals to $\hat{m}_{red}$ at the end of the reduction period.

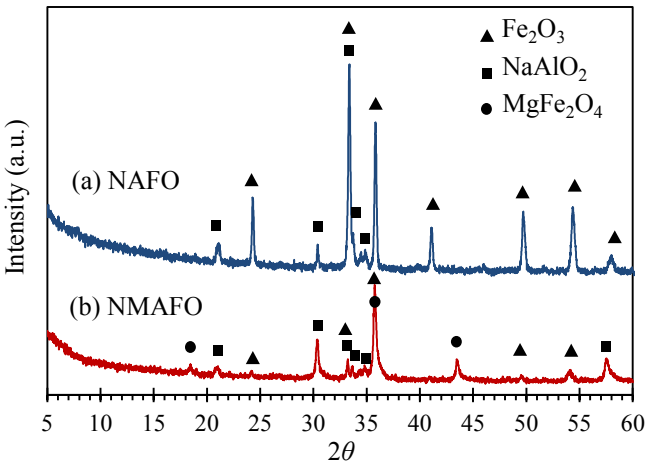

Fig. 4 XRD patterns of the freshly-prepared oxygen carriers of (a) NAFO and (b) NMAFO.

Table 1. Results of the elemental analysis of the freshly-prepared oxygen carriers by XRF, on oxide basis and metal basis. Contaminants include oxides of Ca, Cr, and Si.

XRF analysis, oxide basis (wt%)					
	Fe_2O_3	Al_2O_3	Na_2O	MgO	Contaminants
NAFO	64.3	20.7	12.2	0	2.8
NMAFO	51.7	25.2	10.7	10.2	2.1
XRF analysis, metal basis (mol%)					
	Fe	Al	Na	Mg	Contaminants
NAFO	48.9	24.7	23.9	0	2.5
NMAFO	36.4	27.8	19.4	14.4	2.0

Accordingly, $x_{Fe_2O_3}$ for NAFO and NMAFO were found to be 64.7 and 49.3 wt%, respectively. Both values are lower than those calculated in section 2.1, assuming the oxygen carriers contain only oxides of Mg^{2+}, Al^{3+} and Fe^{3+}. Therefore, the results of the thermogravimetric analysis indicate that both oxygen carriers contain substantial amount of Na^+.

The compositions of the crystalline phases of the calcined oxygen carriers were investigated by XRD, the patterns of which are plotted in Fig. 4. In Fig. 4, NAFO was found to contain Fe_2O_3 and $NaAlO_2$. For NMAFO, phases of Fe_2O_3 (haematite), $NaAlO_2$ and $MgFe_2O_4$ were found. Interestingly, the product of the possible interaction between MgO and Al_2O_3, *viz*. $MgAl_2O_4$, which would generate strong diffraction peaks at *e.g.* 36.9° and 44.9°, was not detected.

In addition to XRD, the elemental composition of the oxygen carriers was quantified by XRF, and results are shown in Table 1. From Table 1, it can be seen that the ratio of [Na] and [Al] is very close to unity in NAFO, indicating that almost all Al^{3+} precipitated in the form of $NaAlCO_3(OH)_2$. The ratio of Fe: Al in the freshly-prepared NAFO was found to be ~2, higher than the expected value of 1.49, suggesting some loss of Al^{3+} during preparation. This could be a result of Al^{3+} in the precipitate re-dissolving under an alkaline environment by:

$$Al(OH)_{3(s)} + H_2O_{(l)} \leftrightarrow [Al(OH)_4]^-_{(aq)} + H^+_{(aq)}, \text{ or} \quad (13)$$

$$NaAlCO_3(OH)_{2(s)} + 2H_2O_{(l)} \leftrightarrow Al(OH)_4^-{}_{(aq)} + HCO_3^-{}_{(aq)} + Na^+_{(aq)} + H^+_{(aq)}, \quad (14)$$

during aging and probably washing. Table 1 also shows that the ratio of [Mg]: [Al]: [Fe] in the freshly-calcined NMAFO is 1: 1.9: 2.5, which suggests some loss of Mg^{2+} and Al^{3+} during synthesis. However, the ratio of [Mg]: [Al] in NMAFO remains roughly the same as its nitrate precursor, in which [Mg]: [Al]: [Fe] = 1: 2: 2.16. Apart from the major metal elements *viz*. Na^+, Fe^{3+}, Al^{3+} and Mg^{2+} in the case for NMAFO, XRF also detected some contamination by trace elements such as Si, Cr and Ca. The oxides of these contaminants make up less than 2.8 % of the total mass of the oxygen carriers. These contaminants probably come from impurities in the chemical precursors. Based on the results of XRF, NAFO and NMAFO contain, respectively, 64.3 and 51.7 wt% of Fe_2O_3, assuming that the metal oxides are fully oxidised and do not form mixed oxides or solid solutions. Here, a solid solution is considered as a single crystal phase, formed from phases with almost identical crystal structure, *e.g.* Fe_3O_4 and $MgFe_2O_4$. The contents of Fe_2O_3 deduced by XRF are very close to those estimated from the TGA in Fig. 3, suggesting that all the Fe(III) in both oxygen carriers is eventually reducible in H_2 to Fe(0). However, the proportion of Fe(III) practically reducible to Fe(0) during chemical looping is discussed in section 5.2, below.

5.2. Cyclic performance in chemical looping

Particles of both oxygen carriers, sized d_p = 300-425 μm, were investigated in a packed bed for the chemical looping production of hydrogen at 1123 K. As mentioned above, the production of hydrogen was simulated by the production of CO by oxidising the reduced oxygen carrier in CO_2, the redox potential of which is almost identical to that of steam at 1123 K. A total of 20 cycles were performed in each experiment. Profiles of mole fractions of CO and CO_2 in the

off-gas during the first two cycles as well as the last cycle in a typical cycling experiment are shown in Fig. 5. Here, the concentration of O_2 during the air-oxidation was not measured. It can be seen from Fig. 5 that, in the case of NMAFO, the profiles were reproducible over the cycles, showing stable performance. The profile of CO_2 produced during reduction, when CO was fed to the inlet, showed an initial sharp rise followed by decay. This is characteristic of the reduction of Fe_2O_3 successively to Fe_3O_4, FeO and Fe.[19] It should be noted that the concentration of CO_2 did not fall to zero at the end of the reduction, suggesting a conversion of Fe_2O_3 to metallic Fe of less than 100% in each cycle. On the other hand, the rate of oxidation of the reduced carriers by CO_2 fell to zero after 90 s, suggesting fast apparent rates *c.f.* reduction. The spike of CO_2 at the very beginning of the oxidation in each cycle was a result of insufficient mixing between CO_2 and N_2 in the feed, immediately after gas-switching, which was achieved using solenoid valves.

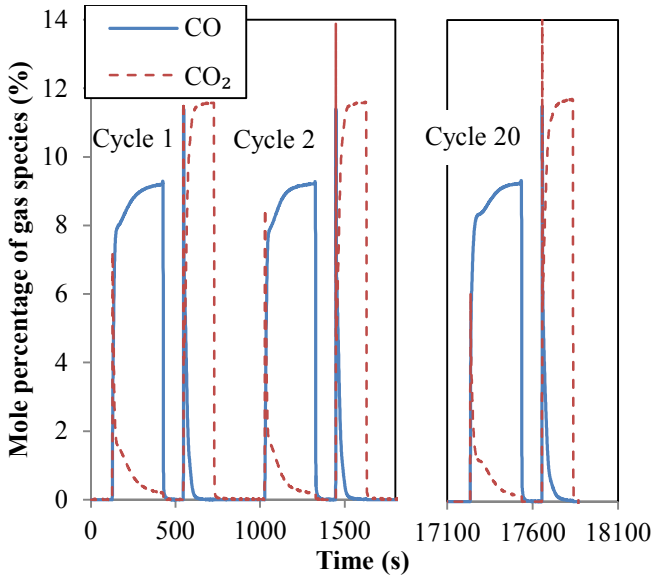

Fig. 5 Variation of the mole fractions of CO and CO_2 in the off-gas of a packed bed, in which a small amount of NMAFO was cycled at 1123 K under conditions equivalent to those suitable for producing hydrogen by chemical looping. The oxygen carrier is tested for 20 cycles, where the profiles of the first two cycles and the last cycle are shown here. The packed bed was oxidised in air at the end of each cycle, although the concentration of oxygen is not measured during the experiments.

The conversion from Fe_3O_4 to Fe, X, was calculated in two ways, when the oxygen carriers were oxidised in air to Fe_2O_3 at the end of each cycle:

$$X_{\text{red}} = \frac{1}{0.01667}\left(\frac{\dot{N}_{\text{CO+N}_2}}{m_0 x_{\text{Fe}_2\text{O}_3}}\int_0^{300} y_{\text{CO}_2}\,dt - 0.00208\right), \qquad (15)$$

$$X_{\text{ox}} = \frac{1}{0.01667}\frac{\dot{N}_{\text{CO}_2+\text{N}_2}}{m_0 x_{\text{Fe}_2\text{O}_3}}\int_{540}^{720} y_{\text{CO}}\,dt\,. \qquad (16)$$

Here, equations (15) and (16) calculate X during the reduction and the subsequent CO_2-oxidation, respectively. The constants 0.00208 and 0.01667 mol are the stoichiometric amounts of CO_2 produced, per g of Fe_2O_3, for the complete reduction from Fe_2O_3 to Fe_3O_4 and from Fe_3O_4 to Fe, respectively; $\dot{N}_i$ is the molar flowrate of species i through the packed bed, y_i is the measured mole fractions of species i and $x_{\text{Fe}_2\text{O}_3}$ is the mass fraction of Fe_2O_3 (assuming all Fe is in the form of Fe_2O_3) in the fully-oxidised sample. Finally, m_0 is the mass in g of the oxygen carrier in its fully-oxidised state and t is time in s, counting from the first instance when CO was fed to the bed in each cycle. In cases where the bed was not oxidised in air, an alternative expression:

$$X_{\text{red}} = \frac{1}{0.01667}\frac{\dot{N}_{\text{CO+N}_2}}{m_0 x_{\text{Fe}_2\text{O}_3}}\int_0^{300} y_{\text{CO}_2}\,dt \qquad (17)$$

was used to calculate X_{red}. It should be emphasised that, in this study, X is a measure of the oxygen carrier's ability to generate hydrogen, *i.e.* the yield of hydrogen in each cycle, if steam is used as an oxidant. A value of X equal to unity means that all Fe-containing species can be reduced fully to Fe and then oxidised to Fe_3O_4 by steam, giving 100% yield of hydrogen. Equation (15) also assumes that Fe_2O_3 must be reduced fully to Fe_3O_4 prior to further reduction to FeO and Fe.

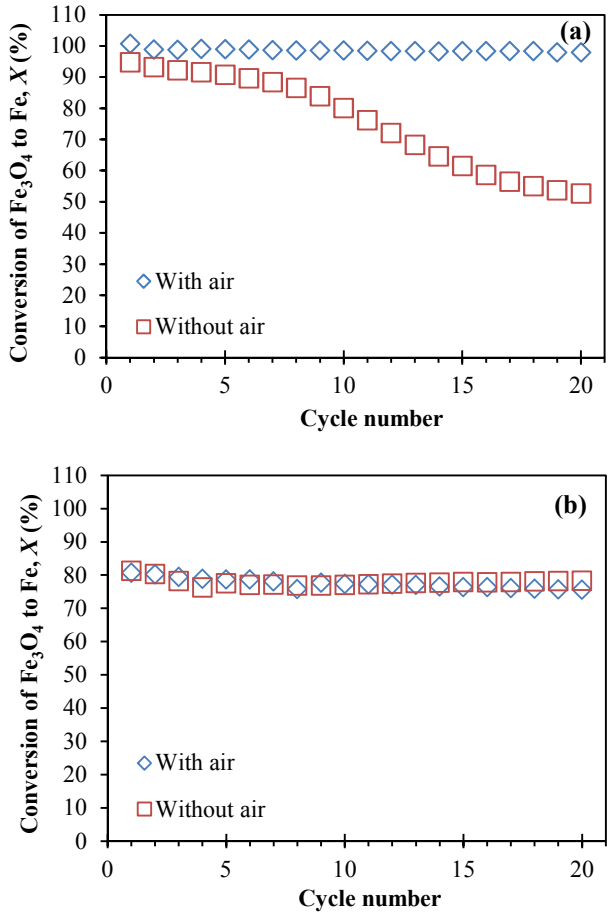

Fig. 6 The conversion of Fe_3O_4 to Fe, X versus cycle number, when approximately 0.3 g of (a) NAFO and (b) NMAFO were cycled in a packed bed reactor in the presence or absence of oxidation by air, at 1123 K. Error bars are too small to be shown here.

The calculated results of X_{red} and X_{ox} in each cycle typically differ by less than 1%. Therefore, the arithmetic mean of X_{red}

and X_{ox} was taken as the average value of X in each cycle. The measured X were plotted against cycle number in Fig. 6. Fig. 6 (a) shows that, when NAFO was oxidised by air at the end of each cycle, $X \sim 100\%$ consistently over 20 cycles. In contrast, without air, X fell quickly, tending towards 50% by the 20th cycle. This diminution is similar to those reported by Bohn *et al.*[5] and Kidambi *et al.*[7], who studied oxygen carriers made of Fe_2O_3 and Al_2O_3 for chemical looping production of hydrogen and attributed the decaying conversion to the formation of $FeAl_2O_4$. Furthermore, Kidambi *et al.*[7] hypothesised two possible reasons for this reduced yield: (i) the presence of the alumina alters the equilibrium for the reduction of iron oxide, making it effectively harder to reduce and (ii) the Fe-Al-O mixture could not prevent sintering over repeated cycles owing to the lack of cyclic phase segregation. In contrast, more consistent performance was seen for NMAFO, as shown in Fig. 6b, regardless of whether or not air oxidation was used. The measured X, with and without air, equals to *ca.* 80% over the 20 cycles at 1123 K. These values of X were less than unity owing to the fact that reduction did not reach completion in each cycle, as discussed above.

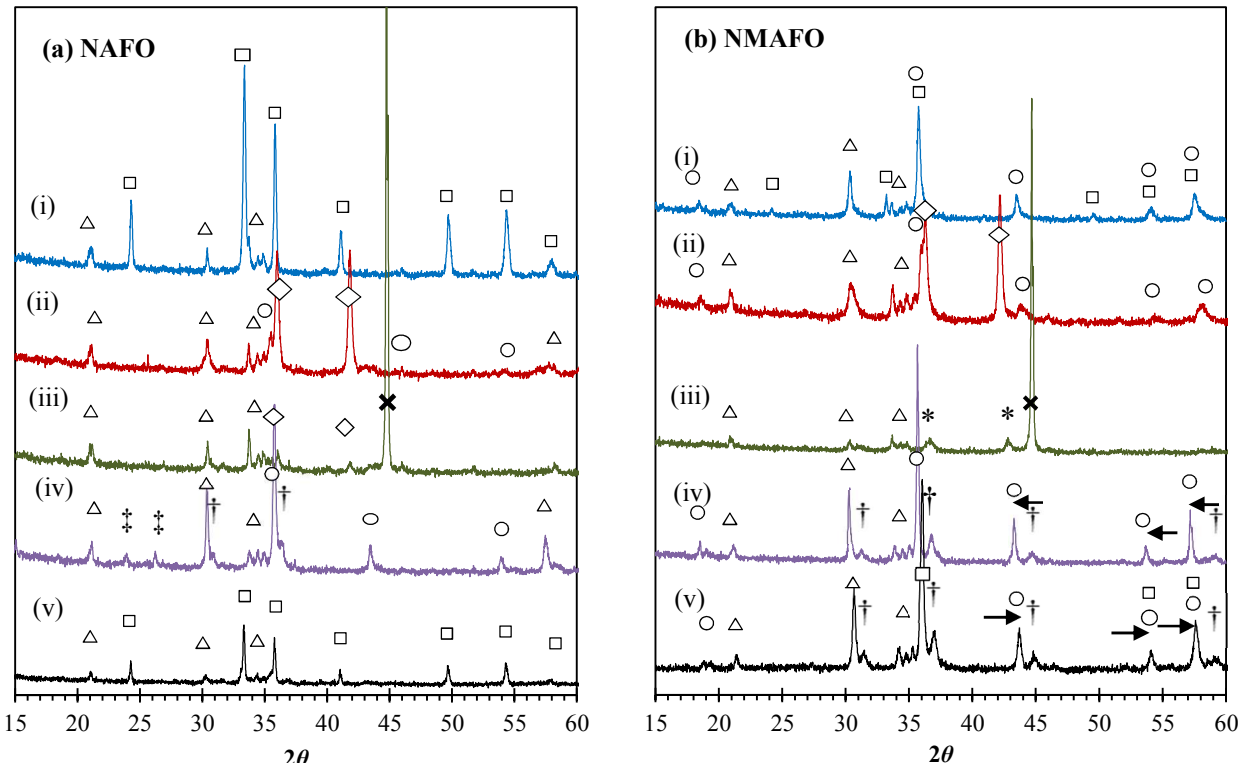

Fig. 7 XRD patterns of (a) NAFO and (b) NMAFO at different stages of the cycling experiments, when they are (i) fresh, (ii) reduced in a mixture of CO and CO_2 (p_{CO_2}:p_{CO} = 1) at 1123 K for 10 min, (iii) reduced in 10% CO in N_2 at 1123 K for 10 min, (iv) oxidised in CO_2, after 20 cycles without oxidation in air, and (v) oxidised in air, after 20 cycles with oxidation in air. All peaks are assigned and labelled: △ $NaAlO_2$, □ Fe_2O_3, ○ Fe-based spinel (*e.g.* Fe_3O_4 and, or $MgFe_2O_4$), ◇ wüstite, * MgO, × Fe, and † Al-based spinel (*e.g.* $MgAl_2O_4$ and, or $FeAl_2O_4$). The peaks marked by ‡ are not indexed. The arrows indicate peak-shifts relative to a pure phase of $MgFe_2O_4$.

Fig. 7 shows the XRD patterns of the oxygen carriers before and after cycling, as well as the fresh samples after various treatments, *viz.* (i) reduction in 10% CO in N_2 at 1123 K for 10 min and (ii) reduction in a mixture of CO and CO_2 (p_{CO_2}:p_{CO} = 1) at 1123 K for 10 min. For NAFO, it can be seen from Fig. 7 (a) that, during the reduction of the fresh oxygen carrier, the Fe_2O_3 is reduced subsequently to Fe_3O_4, FeO and finally Fe, without any detectable formation of $FeAl_2O_4$, *i.e.* the interaction between FeO and Al_2O_3 was absent during the first cycle, and hence the initially high X seen in Fig. 6(a). However, peaks of FeAl2O4 can be clearly seen in the sample after 20 cycles without air-oxidation Fig. 7 (a)(iv)). This result suggests that there was an accumulation of $FeAl_2O_4$ in NAFO over cycles without air-oxidation. Consequently the reactivity of the oxygen carrier decreases gradually and progressively, as seen in Fig. 6(a). Finally, the two diffraction peaks between 21° and 26° seen in Fig. 7 (a)(iv) could not be adequately fitted by Rietveld refinement. With air-oxidation, no $FeAl_2O_4$ is found after cycling, *i.e.* $FeAl_2O_4$ could not accumulate. When fully oxidised in air, the cycled material has a diffraction pattern Fig. 7 (a)(v) almost identical to that of the fresh NAFO Fig. 7 (a)(i). These XRD patterns suggest that the formation of $FeAl_2O_4$ in NAFO was a slow and irreversible process in the absence of air-oxidation, but could be reserved by oxidising the oxygen carrier in air at the end of each cycle. In addition, the $NaAlO_2$ phase was detected consistently during the reduction and after 20 cycles, indicating it is relatively stable under the conditions used in this study.

The XRD patterns of NMAFO at various stages of the cycling experiment are shown in Fig. 7 (b). Here, attention is given to

the spinel compounds of Fe_3O_4 and $MgFe_2O_4$, which are mutually soluble and have similar diffraction patterns. For example, the (4 0 0) plane of Fe_3O_4 produces a peak at 43.1° whereas for $MgFe_2O_4$ the (4 0 0) peak is at 43.2°. On the other hand, the solid solution of $MgFe_2O_4$ and Fe_3O_4 can be easily distinguished from the alumina-based spinel phases of $FeAl_2O_4$ and $MgAl_2O_4$, the (4 0 0) reflections of which show peaks 44.4° and 44.9°, respectively. The differences between the positions of corresponding peaks are greater at higher angles according to Bragg's Law. Fig. 7 (b)(i) shows that the fresh oxygen carrier consists of a mixture of Fe_2O_3, $MgFe_2O_4$ (possibly with a small amount of Fe_3O_4) and $NaAlO_2$. Looking at the position of the peaks of Fe_2O_3 and $MgFe_2O_4$, there is no strong evidence to suggest that either phase forms a solid solution with Al_2O_3 in the fresh NMAFO. After reduction in an equimolar mixture of CO_2 and CO (Fig. 7 (b)(i)) at 1123 K, the peaks of $MgFe_2O_4$ weaken and those of wüstite start to appear (Fig. 7b(ii)). After reduction in CO for 10 min, the crystalline phases detectable are MgO, Fe and $NaAlO_2$ (Fig. 7 (b)(iii)). During the reduction of fresh NMAFO, $NaAlO_2$ appeared to be the only crystalline phase that contains Al(III), despite the fact that there is more Al than Na in NMAFO. After 20 cycles at 1123 K without air-oxidation (Fig. 7 (b)(iv)), the oxygen carrier is found to contain $MgFe_2O_4$, Fe_3O_4, $MgAl_2O_4$ and $NaAlO_2$, where the presence of Fe_3O_4 is manifested by the peaks of $MgFe_2O_4$ shifting slightly to a lower 2θ value. With air-oxidation, the XRD pattern of the fully oxidised sample (Fig. 7 (b)(v)) shows the same phases as Fig. 7 (b)(iv), but with an additional phase of Fe_2O_3. In Fig. 7b(v), the positions of peaks of Fe_2O_3 and $MgFe_2O_4$ are slightly shifted to the right, suggesting the partial dissolution of Al^{3+} in both phases. The dissolution of Al^{3+} in $MgFe_2O_4$ is not obvious in Fig. 7b(iv), because the effect of shift of peaks of $MgFe_2O_4$ due to Al^{3+} might have been cancelled by the opposite effect due to Fe_3O_4. Overall, the evolution of the XRD patterns in Fig. 7b shows that, the $MgFe_2O_4$ phase (with some dissolved Fe_3O_4) was decomposed during reduction, and could be regenerated in CO_2. Despite the formation of $MgFe_2O_4$, the nearly 80% X seen in Fig. 6(b) demonstrates that this spinel compound did not significantly compromise the reactivity of Fe_2O_3. In addition, the fact that $MgFe_2O_4$ may be regenerated in CO_2 means there is a potential to produce more hydrogen per mole of Fe by the steam-oxidation of reduced $MgFe_2O_4$ than of pure Fe; this is discussed below in section 6.2. Lastly, similar to the case of NAFO, $NaAlO_2$ was deemed stable under the conditions used for the cycling tests.

Another important aspect indicating the stability of an oxygen carrier is its change in surface morphology with redox cycling. This was investigated by SEM; the results in Fig. 8 show the morphologies of NAFO when (a) fresh, (b) after 20 cycles without air-oxidation and (c) after 20 cycles with air-oxidation, respectively, as well as the surface of particles of NMAFO when (d) fresh and (e) + (f) after 20 cycles without oxidation in air. In all cases, the disappearance of the rod-shaped grains seen in Fig. 2 can be correlated to the decomposition of dawsonite ($NaAlCO_3(OH)_2$). Fig. 8(a) shows that fresh NAFO, the surface of which is relatively porous, is composed of small, irregularly-shaped grains of uniform size. After 20 cycles without air-oxidation, some large hexagonal crystals were found in NAFO, together with some agglomerated small grains of no particular crystalline feature. When cycled with air-oxidation, the surface of NAFO was found to be mainly composed of uniformly-sized grains similar to those seen in Fig. 8 (a). A large grain exhibiting a prismatic crystal habit is also seen in Fig. 8(c); this means that the crystallite has an orthorhombic crystal structure, suggesting that it is made of $NaAlO_2$. On the other hand, both fresh and cycled (without air-oxidation) NMAFO were found to contain large hexagonal crystals of *ca.* 1 µm in size mixed with small grains of *ca.* 100 nm in size. Interestingly, none of the crystalline phases identified in Fig. 7 (b)(iv) crystallises hexagonally. To investigate the nature of the hexagonal crystals seen in energy-dispersive X-ray spectra (EDS) of the corresponding samples were taken at points shown in Fig. 9; and the results of the quantitative analysis are presented in Table 2.

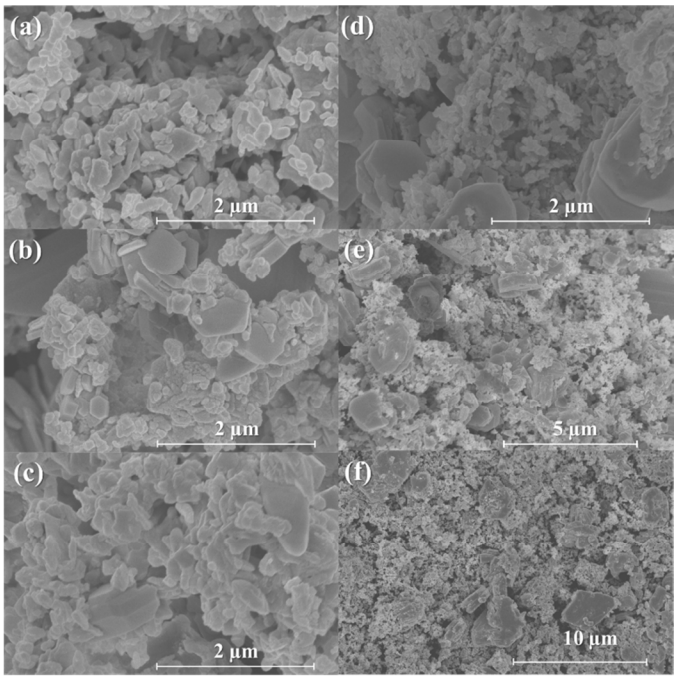

Fig. 8 SEM images of (a) Fresh NAFO; (b) NAFO after 20 cycles without air-oxidation; (c) NAFO after 20 cycles with air-oxidation; (d) fresh NMAFO; and (e) and (f) NMAFO after 20 cycles without air-oxidation at different magnifications.

Here, it should be noted that, the volume of interaction between the electron beam (with an accelerating voltage of 15 kV) and the solid material is several microns wide. Hence, the EDS collected for the hexagonal grains, *e.g.* spectra 2, 10 and 11, might also contain signals produced by the surrounding materials. Therefore, the numbers shown in Table 2 should only be regarded as giving a qualitative indication, which can only be used to estimate the chemical compositions of the hexagonal grains, in combination with other experimental results.

The result of EDS analysis (Fig. 9 and Table 2) suggests that these micron-sized hexagonal grains are predominantly made of Al_2O_3, which means that the "host-phase" of these crystals could be corundum (α-Al_2O_3), β-alumina ($(Na_2O)_n \cdot (Al_2O_3)_{11}$, where $n = 1 - 1.5$), or β"-alumina ($(Na_2O) \cdot (Al_2O_3)_6$). However, the lack of detection of the corundum peaks in Fig. 7 suggests that, the content of Al_2O_3 relative to the other phases is low in the bulk of the solid, despite its strong presence at the surface. Furthermore, the strongest peak of Al_2O_3 at around 35° could overlap with a peak of $NaAlO_2$, making detection of the former even more difficult. From Fig. 9 and Table 2, it can be also seen that, the metal-based elemental composition of the small, 100 nm-sized grains in NAFO was comparable to the analysis by XRF, although the content of Fe in the small grains in NMAFO appears to be underestimated by EDS.

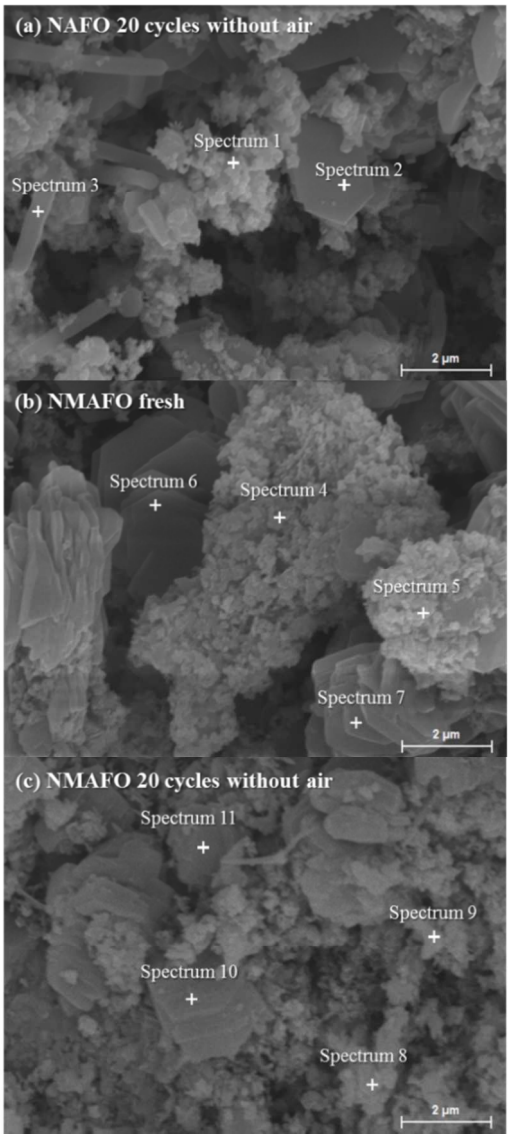

Fig. 9 SEM image of the surface of a particle of (a) NAFO after 20 cycles without oxidation by air, (b) fresh NMAFO and (c) NMAFO after 20 cycles without oxidation by air. Positions where EDS spectra were taken are marked by crosses and results are shown in Table 2.

6. Discussion

6.1. Performance of NAFO

The experimental results suggest that NAFO underwent several phase changes during its initial preparation and also during the subsequent cycling experiments. The interesting features observed during the experimental investigation of NAFO are discussed in this section.

6.1.1. Behaviour of NAFO during redox cycling without an air-oxidation step

Unfortunately, a comprehensive phase diagram for the Na-Fe-Al-O system is not available in the literature, so that the following discussion is based on experimental results from both the current study as well those in the existing literature.

Firstly, the chemical inertness of the $NaAlO_2$ phase was investigated by XRD for $27° \leq 2\theta \leq 33°$, with a slow scanning speed of 0.00418° per 50 s per step. The results of the XRD, shown in Fig. 10, indicate that for both NAFO and NMAFO, the (1 2 0) peak of the $NaAlO_2$ phase at 30.3° has shifted slightly to a lower 2θ value after the cycling experiments. Here, the $NaAlO_2$ originates from the dawsonite in the original precipitation. This shift could be explained by the dissolution of Fe^{3+} into the $NaAlO_2$ phase, forming a solid solution with a general formula $NaAl_{1-y}Fe_yO_2$ ($0 < y < 1$), which is stable even at room temperature.[20] However, Fig. 2(a) suggests, visually, that $Fe(OH)_3$ and dawsonite ($NaAlCO_3(OH)_2$) precipitated heterogeneously during the preparation of NAFO, so that for Fe^{3+} - from either Fe_2O_3 or Fe_3O_4 - to dissolve in the $NaAlO_2$ phase, it would have to migrate a considerable distance to do so. Because the migration of ions in a solid is often a slow process below its melting point, the substitution of Al^{3+} by Fe^{3+} in $NaAlO_2$ might therefore be, kinetically, slow, even though thermodynamically favourable.

Table 2: Results of quantitative analysis of EDS spectra taken at points shown in Fig. 9. The compositions of the metal elements are presented in normalised mol%, excluding signals due to C, O and the Pt coating.

	NAFO 20 cycles without air-oxidation			NMAFO fresh				NMAFO 20 cycles without air-oxidation			
Spectrum	1	2	3	4	5	6	7	8	9	10	11
Al (mol%)	23	52	21	30	31	87	80	22	38	79	74
Fe (mol%)	63	28	44	26	24	6	10	21	27	15	10
Mg (mol%)	0	0	0	19	19	1	2	20	23	3	9
Na (mol%)	14	21	35	25	26	6	8	38	13	3	6

Thus, a plausible explanation to the behaviour of the oxygen carrier is proposed and depicted in Fig. 11. Here, the reaction schematic shown in Fig. 11 postulates that, as a result of the formation of $NaAl_{1-y}Fe_yO_2$, where y increased gradually with time, an increasing amount Al^{3+} was displaced from the

$NaAl_{1-y}Fe_yO_2$ phase, and became free to interact with oxides of Fe. Evidence for this explanation comes from XRD measurements on fresh carrier and carrier cycled many times. Initially, the freshly-calcined oxygen carrier contained a mixture of $NaAlO_2$ and Fe_2O_3, both of which were detected by XRD, as seen in Fig. 7 (a)(i). In the first cycle, the only reactive species in the fresh NAFO was Fe_2O_3, whilst the $NaAlO_2$ was more or less stable, as seen in Fig. 7 (a), (i)-(iii). In other words, almost all the Fe^{3+} in NAFO was present as Fe_2O_3, which could be reduced completely to Fe, resulting in the observed X of ~ 100%. However, peaks of $FeAl_2O_4$ can be clearly seen in the sample after 20 cycles without air-oxidation (Fig. 7 (a)(iv)), suggesting that a substantial amount of Al^{3+} was made available to interact with Fe_2O_3, Fe_3O_4 and FeO. In particular, the formation of $FeAl_2O_4$ has been known to be responsible for the decaying performance of the Fe-based oxygen carriers in the absence of an air-oxidation step.[6,7] Thus far, the theory matches the experimental facts.

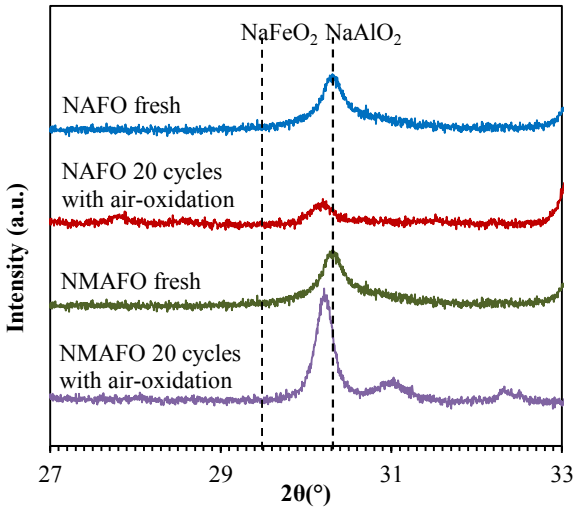

Fig. 10 X-ray diffraction patterns of the oxygen carriers before and after the cycling experiments, when they are fully oxidised in air and cooled to room temperature. Calculated peak positions of the (1 2 0) reflection for both $NaFeO_2$ and $NaAlO_2$ are marked with dashed lines.

6.1.2. Behaviour of NAFO during redox cycling with an air-oxidation step.

This section considers the picture when there is air oxidation included in each cycle and how the mechanism just posited is altered; this is also depicted in Fig. 11. Firstly, despite an increasing value of y in the $NaAl_{1-y}Fe_yO_2$ phase, the consistently high conversion over the 20 cycles with air-oxidation shown in Fig. 6(a) means that, the accumulation of Fe^{3+} in $NaAl_{1-y}Fe_yO_2$ by itself was not deleterious to the reactivity of the oxygen carrier, and that the Fe^{3+} in $NaAl_{1-y}Fe_yO_2$ could be fully reduced and oxidised in each cycle. Here, it should be remembered that the Fe^{3+} in the $NaAl_{1-y}Fe_yO_2$ phase is stable in CO_2 or H_2O and cannot be oxidised further. Secondly, Bohn *et al.*[5] and Kidambi *et al.*[7] showed that the decay in performance of the Fe_2O_3-Al_2O_3 based oxygen carriers can be minimised by oxidation in air at the end of every cycle, an observation reinforced by the results in Fig. 6(a). Kidambi *et al.*[7] showed further that the unreactive spinel, $FeAl_2O_4$, formed by the interaction within the Fe-Al-O system, could be eliminated by oxidation with air because, with such treatment, any $FeAl_2O_4$ formed decomposed to alumina and haematite, and simple solid solutions thereof, in line in fact with the thermodynamic predictions from the Fe-Al-O phase diagram. Accordingly, it is concluded that (i) the addition of Na_2O alone to a mixture of Fe_2O_3 and Al_2O_3 is insufficient to prevent the Fe-Al-O interaction, and (ii) the accumulation of the resulting $FeAl_2O_4$ spinel will lead to a progressive reduction in reactivity unless it is decomposed by air-oxidation in each cycle.

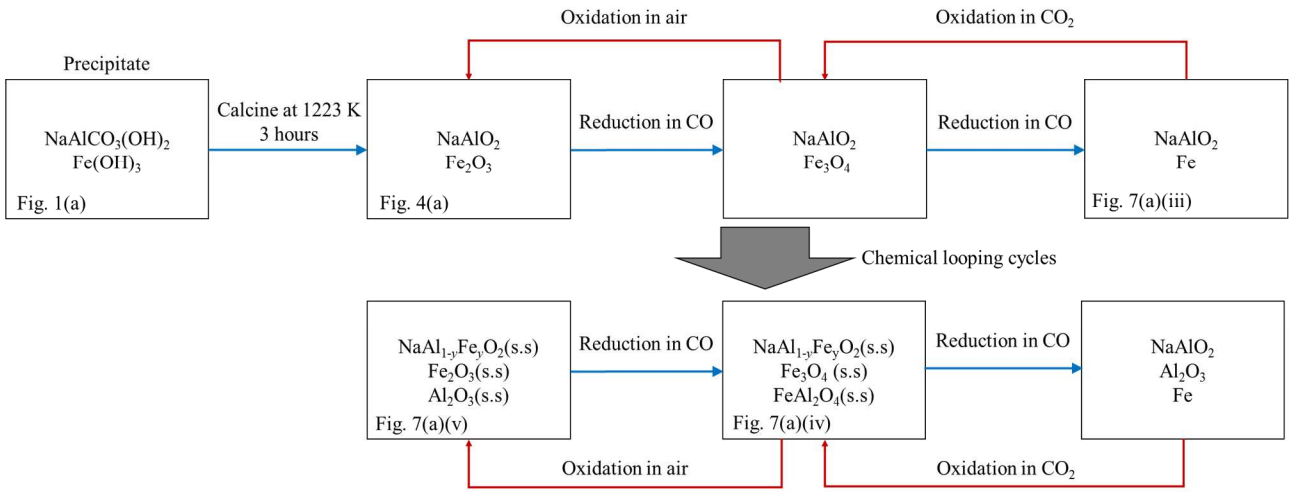

Fig. 11 A schematic diagram showing the change of composition of the oxygen carrier NAFO at various stages of the experimental investigation. The availability of the corresponding XRD patterns is denoted at the bottom of the boxes.

RSC Advances RSCPublishing

ARTICLE

6.2. Performance of NMAFO

Here, the changes in composition during the preparation and investigation of NMAFO are depicted in Fig. 12 and discussed below. In NMAFO, MgO has been added to the oxygen carrier such that [Mg]:[Al] = 0.5, a ratio theoretically sufficient to bind all the Al_2O_3 in the form of $MgAl_2O_4$, even if no sodium aluminate phase forms. The results of XRF, shown in Table 1, indicate that in NMAFO the ratio [Al]:[Na] is >> 1. Therefore, besides $NaAlO_2$, there should be at least one more Al-containing phase present in the freshly-calcined oxygen carrier. The results of EDS analysis, shown in Fig. 9 and Table 2, suggest that this Al-containing phase could be Al_2O_3 (corundum), which appears to be stable in the form of large hexagonal crystals before and after the cycling experiments, with or without air-oxidation. In addition, the absence of $MgAl_2O_4$ peaks in Fig. 7 (b)(i)-(iii), and the absence of cubic crystals in Fig. 8 (d), suggest that the fresh NMAFO contains very little $MgAl_2O_4$.

As with NAFO, $NaAl_{1-y}Fe_yO_2$ was progressively formed with cycling and its presence verified by XRD, with evidence shown in Fig. 10. Therefore, analogous to the case for NAFO, it is suggested here that the initially pure $NaAlO_2$ phase is gradually doped with Fe^{3+}, progressively forming $NaAl_{1-y}Fe_yO_2$ over the course of the cycling experiments. Then, the displaced Al^{3+} ions are simultaneously absorbed by: MgFe2O4 + Al2O3 = MgAl2O4 + Fe2O3. Consequently, MgAl2O4 accumulated over time, and is clearly seen in Fig. 7 (b)(iv) and (v). In the extreme scenario where all the Al^{3+} ions are eventually displaced by Fe^{3+} in the $NaAl_{1-y}Fe_yO_2$ phase, a ratio of [Mg]: [Al] of 0.5 would ensure that $FeAl_2O_4$ does not form. Hence, the oxygen carrier showed consistent conversion from Fe_3O_4 to Fe of ~80% with or without air-oxidation over 20 cycles at 1123 K. In passing, it should be also noted that the conversion is less than unity in Fig. 6(b) because the reduction was not completed in each cycle, as indicated by the non-zero $[CO_2]$ at the end of each reduction step in Fig. 5.

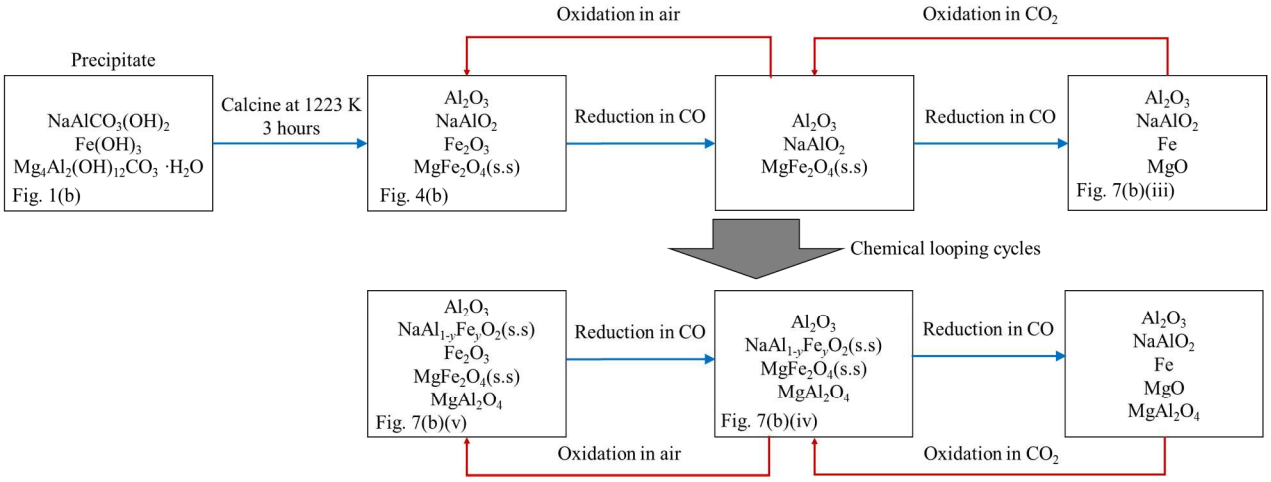

Fig. 12 A schematic diagram showing the change of composition of the oxygen carrier NMAFO at various stages of the experimental investigation. The availability of the corresponding XRD patterns is denoted at the bottom of the boxes.

Prior to the formation of $MgAl_2O_4$, all the MgO is assumed to be present in the form of $MgFe_2O_4$, as shown in Fig. 12. Thus, the reactive phases in the freshly-calcined NMAFO should be, by simple stoichiometry, a mixture of 51.0 wt% $MgFe_2O_4$ and 13.9 wt% Fe_2O_3, with a ratio of [Fe]/([Fe] + [Mg]) ~ 0.73, together with $NaAlO_2$, which remains effectively stable during the first cycle. After cycling, the XRD patterns in Fig. 7 (b) (iv) and (v) suggest that there remains substantial amounts of $MgFe_2O_4$. In contrast with $FeAl_2O_4$, the spinel $MgFe_2O_4$ formed in NMAFO appeared to be readily reducible under the conditions of experimentation used and so its formation did not lead to a fall in the reactivity of NMAFO.

The phase diagram of the Mg-Fe-O system at 1123 K, calculated using MTDATA[21] and plotted in Fig. 13, can be used to explore the thermodynamics further. Fig. 13 shows that, in the Mg-Fe-O system, the reduction of NMAFO, in which Fe/(Fe+Mg) > 0.68, involves three phase transitions: (i) haematite to $MgFe_2O_4$-Fe_3O_4 solid solution, (ii) $MgFe_2O_4$-Fe_3O_4 solid solution to MgO-FeO solid solution, and (iii) MgO-FeO solid solution to metallic Fe. These three phase transitions are analogous to the three phases in the reduction of

Fe_2O_3 sequentially to Fe_3O_4, FeO and Fe. However, in the presence of Mg^{2+}, the phase transitions from haematite to spinel (Fe_3O_4 and $MgFe_2O_4$) and then to halite (MgO and FeO) occur at higher values of equilibrium p_{O_2} than for the corresponding transitions with pure iron oxides. Thus, thermodynamically, the MgO-Fe_2O_3 mixture could in fact be more readily reducible than pure Fe_2O_3. On the other hand, in a commercial chemical looping process, where the reduced oxygen carrier is oxidised by steam, the hydrogen produced by the reduced NMAFO would be more dilute than that by pure Fe, because of the shifted-equilibrium; this is a potential drawback because more steam is needed for each mole of hydrogen produced using NMAFO. Another implication of the Mg-Fe-O phase diagram is that, in NMAFO, a larger proportion of Fe could be oxidised to Fe(III) by steam than for pure Fe_2O_3. However, taking into account the dilution by MgO, the theoretical yield of hydrogen per unit mass of fully-oxidised oxygen carrier, for any $MgFe_2O_4$-Fe_2O_3 mixture, is still lower than that for unmodified Fe_2O_3. To investigate the assertions mentioned above, the behaviour of a mixed oxide containing only Mg and Fe, *e.g.* $MgFe_2O_4$, should be studied in future work. Interestingly, a molar ratio of Mg:Fe:Al = 3.5: 6: 1 could be fruitful in future investigations, because such a composition corresponds to an oxygen carrier consisting of $MgFe_2O_4$ (as an active component) and $MgAl_2O_4$ (as a support). Thus, the use of Mg^{2+} as an inhibitor as well as a promoter might be optimised.

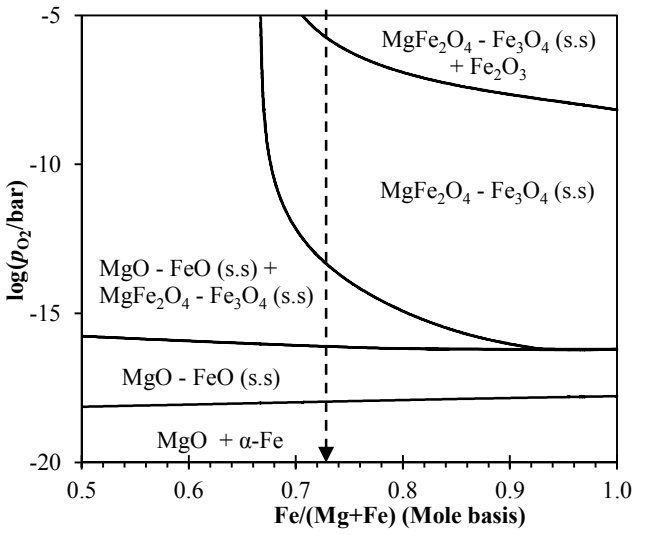

Fig. 13 Calculated phase diagram of the Mg-Fe-O showing log(p_{O_2}/bar) versus cationic mole fraction of Fe at 1123 K, at the Fe-rich side. The dashed line marks the molar ratio of Fe: (Fe + Mg) ~ 0.73 in NMAFO.

Finally, Fig. 13 shows that, during the cycling experiments, the $MgFe_2O_4$-Fe_2O_3 mixture in NMAFO would be transformed between single-phase regions and two-phase mixtures repeatedly. It is believed that cycling between a two-phase mixture and a single-phase solid solution could give oxygen carriers a regenerable porous structure, which renders superior cyclic stability over conventional oxygen carriers, *e.g.* metal oxides mixed with catalyst supports.[7,22] Dunstan *et al.*[22] have suggested that a similar mechanism might explain the longevity of their high-temperature sorbents for the capture and release of CO_2, where the solid sorbents undergo changes in molar volume cyclically at a temperature similar to that used in this study. Nevertheless, it must be remembered that, in practice, the oxygen carrier would have to withstand several thousand of cycles of reduction and oxidation. Therefore, other properties, such as resistance against fracture due to repeated change in molar volume and resistance against attrition, must be considered for the future development of the oxygen carrier.

In conclusion, the oxygen carrier NMAFO worked well, probably because (i) the interaction involving Fe-Al-O was prevented by the formation of $MgAl_2O_4$ and (ii) the thermodynamic properties of the Mg-Fe-O system were utilised, in which the formation of spinel phase and various solid solutions might have improved the "reducibility" of the Fe-based oxygen carriers. This contrasts with the decaying reactivity seen in the Fe-Al-O system.

In the light of the above results , it would also be interesting to investigate the potential use of other elements in group II, *e.g.* Ca and Sr, as well as other divalent metal oxides, to stabilise a mixture of Fe-Al-O and to promote the reactivity of oxides of Fe in the chemical looping production of hydrogen. In fact, analogous systems, *viz.* Ni-Fe-O and Co-Fe-O have been studied by Aston *et al.*[23] for the production of hydrogen by chemical looping. Accordingly, Aston *et al.*[23] found that both $NiFe_2O_4$ and $CoFe_2O_4$ could be reduced to FeO at higher p_{CO_2}/p_{CO} than pure Fe_2O_3, but at the cost of a higher equilibrium value of p_{H_2O}/p_{H_2} during the generation of H_2. All of these mixed oxide systems have demonstrated the potential of altering the thermodynamics of conventional oxygen carriers by using mixed oxides for chemical looping, a technique which can be engineered to suit a wide range of chemical processes involving redox reactions.

7. Conclusion

Fe-based oxygen carriers, consisting of oxides of (i) Na, Al and Fe (NAFO) and (ii) Na, Mg, Al and Fe (NMAFO) were synthesised by means of co-precipitation using a technique involving a gradual reduction in the pH of the solution containing the precursor salts. The major components in the precipitates were $Fe(OH)_3$, $NaAlCO_3(OH)_2$ (dawsonite), and in the case of NMAFO, $Mg_4Al_2(OH)_{12}CO_3 \cdot 3H_2O$ (quintinite); the corresponding oxygen carriers were obtained by calcining these precipitates. Such formulations could in theory prevent the formation of $FeAl_2O_4$, by forming instead the thermodynamically more stable $MgAl_2O_4$ and $NaAlO_2$, which could also act as support materials to stabilise the reactivity of the active Fe_2O_3. The spinel $FeAl_2O_4$ leads to a progressive diminution in the yield of hydrogen unless the carrier is fully oxidised on each cycle using air. It was found that, the sodium in NAFO was unable to prevent the interaction between Al_2O_3 and iron oxide, whereas in NMAFO, the excess MgO used assisted in inhibiting the interaction. When cycled under

conditions suitable for producing hydrogen at 1123 K, both oxygen carriers showed stable performance over 20 cycles, demonstrating ~100% and ~80%, respectively, of their theoretical capacities to produce hydrogen, when they were oxidised in air at the end of each cycle. However, without air-oxidation, the performance of NAFO was found to decay with cycling, attributed to the gradual, progressive formation of $FeAl_2O_4$. In contrast, the performance of NMAFO was found to be stable and consistent with cycling regardless of the inclusion of air-oxidation. The experiments suggested that, although there was some evidence that $NaAlO_2$ resisted the formation of $FeAl_2O_4$, this resistance was slowly compromised by the gradual replacement of Al^{3+} by Fe^{3+} in $NaAlO_2$, leading to the formation of "free" Al_2O_3. This alumina reacted with FeO to form the unreactive $FeAl_2O_4$ in NAFO. However, in NMAFO, free alumina was postulated to react preferentially with Mg^{2+} to form $MgAl_2O_4$ instead of $FeAl_2O_4$ spinel. The unique thermodynamic properties of the Mg-Fe-O system might also be responsible for the outstanding performance of the NMAFO oxygen carrier.

Acknowledgements

The authors would like to thank Mr. S.J. Griggs from the Department of Materials Sciences and Metallurgy, University of Cambridge for access to SEM; Prof C.P. Grey from the Department of Chemistry, University of Cambridge for access to XRD; the EPSRC funded National Chemical Database Service hosted by the Royal Society of Chemistry for crystallographic data. Financial support from the Engineering and Physical Sciences Research Council (Grant number: EP/G063265/1) is acknowledged. This work is also funded by the National Research Foundation (NRF), Prime Minister's Office, Singapore under its Campus for Research Excellence and Technological Enterprise (CREATE) programme.

Notes and references

[a] Department of Engineering, Trumpington Street, University of Cambridge, Cambridge, CB2 1PZ, United Kingdom
[b] Department of Chemistry, University of Cambridge, Lensfield Road, Cambridge, CB2 1EW, United Kingdom
[c] Department of Chemical Engineering and Biotechnology, University of Cambridge, New Museums Site, Pembroke Street, Cambridge, CB2 3RA, United Kingdom
[d] Department of Chemical Engineering, Imperial College London, SW7 2AZ, United Kingdom

1. B. C. H. Steele and A. Heinzel, *Nature*, 2001, **414**, 345–352.
2. C. D. Bohn, C. R. Müller, J. P. Cleeton, A. N. Hayhurst, J. F. Davidson, S. A. Scott, and J. S. Dennis, *Ind. Eng. Chem. Res.*, 2008, **47**, 7623–7630.
3. A. Messerschmitt, *US Pat*., 971,216, 1910.
4. H. Reed and H. Berg, *US Pat*. 2,635,947, 1953.
5. C. D. Bohn, J. P. Cleeton, C. R. Müller, S. Y. Chuang, S. A. Scott, and J. S. Dennis, *Energy Fuels*, 2010, **24**, 4025–4033.
6. A. M. Kierzkowska, C. D. Bohn, S. A. Scott, J. P. Cleeton, J. S. Dennis, and C. R. Müller, *Ind. Eng. Chem. Res.*, 2010, **49**, 5383–5391.
7. P. R. Kidambi, J. P. E. Cleeton, S. A. Scott, J. S. Dennis, and C. D. Bohn, *Energy Fuels*, 2012, **26**, 603–617.
8. J. P. E. Cleeton, Ph.D. Thesis, University of Cambridge, 2011.
9. W. Liu, J. S. Dennis, and S. A. Scott, *Ind. Eng. Chem. Res.*, 2012, **51**, 16597–16609.
10. P. Gayán, L. F. de Diego, F. García-Labiano, J. Adánez, A. Abad, and C. Dueso, *Fuel*, 2008, **87**, 2641–2650.
11. H. Jin, T. Okamoto, and M. Ishida, *Ind. Eng. Chem. Res.*, 1999, **38**, 126–132.
12. T. Mattisson, M. Johansson, and A. Lyngfelt, *Energy Fuels*, 2004, **18**, 628–637.
13. Q. Imtiaz, A. M. Kierzkowska, M. Broda, and C. R. Müller, *Environ. Sci. Technol.*, 2012, **46**, 3561–3566.
14. Q. Imtiaz, A. M. Kierzkowska, and C. R. Müller, *ChemSusChem*, 2012, **5**, 1610–1618.
15. Q. Song, W. Liu, C. D. Bohn, R. N. Harper, E. Sivaniah, S. A. Scott, and J. S. Dennis, *Energy Environ. Sci.*, 2012, **6**, 288–298.
16. A. C. Larson and R. B. Von Dreele, *General Structure Analysis System (GSAS)*, Los Alamos national Laboratory Report LAUR 86-748, 2000.
17. B. H. Toby, *J. Appl. Crystallogr.*, 2001, **34**, 210–213.
18. H. Hellevang, J. Declercq, B. Kvamme, and P. Aagaard, *Appl. Geochem.*, 2010, **25**, 1575–1586.
19. W. Liu, J. Yang Lim, M. A. Saucedo, A. N. Hayhurst, S. A. Scott, and J. S. Dennis, *Chem. Eng. Sci.,* 2014*,* **120**, 149-166.
20. R. Davies, A. Dinsdale, J. Gisby, J. Robinson, and S. Martin, *Calphad*, 2002, **26**, 229–271.
21. J. J. Bara, B. F. Bogacz, T. Jaworska, J. Leciejewicz, M. Styczyńska, and A. SzytuŁa, *J. Magn. Magn. Mater.*, 1988, **75**, 73–78.
22. M. T. Dunstan, W. Liu, A. F. Pavan, J. A. Kimpton, C. D. Ling, S. A. Scott, J. S. Dennis, and C. P. Grey, *Chem. Mater.*, 2013, **25**, 4881–4891.
23. V. J. Aston, B. W. Evanko, and A. W. Weimer, *Int. J. Hydrog. Energy*, 2013, **38**, 9085–9096.